Analytical and Bioanalytical Chemistry (2019) 411:581–589
https://doi.org/10.1007/s00216-018-1351-9

RESEARCH PAPER

Adaptation and improvement of an elemental mapping method for lithium ion battery electrodes and separators by means of laser ablation-inductively coupled plasma-mass spectrometry

Patrick Harte[1] · Marco Evertz[1] · Timo Schwieters[1] · Marcel Diehl[1] · Martin Winter[1,2] · Sascha Nowak[1]

Received: 5 June 2018 / Revised: 17 August 2018 / Accepted: 30 August 2018 / Published online: 7 September 2018

Abstract

In this study, laser ablation-inductively coupled plasma-mass spectrometry (LA-ICP-MS) was applied to previously aged carbonaceous anodes from lithium ion batteries (LIBs). The electrodes were treated by cyclic aging in a lithium ion cell set-up with $LiNi_{0.5}Mn_{1,5}O_4$ (LNMO) cathodes and hard carbon (HC)/mesocarbon microbead (MCMB) anodes. An inhomogeneous transition metal deposition pattern could be induced by replacing the spacer in a standard coin cell set-up with a washer. The inhomogeneity pattern matched the dimension of the washer depicted by the hole in the center. These transition metal (TM) patterns were used to optimize higher lateral scanning speeds and frequencies on the spatial resolution of the mapping experiments using LA-ICP-MS. Higher scanning speeds had an observable influence on the resolution of the obtained image and an overall saving of 60% with regard to time and gas consumption could be achieved. Additionally, the optimized method was applied to the cathode and separator in order to visualize the distribution and deposition pattern, respectively.

Keywords Lithium ion battery · LA-ICP-MS · Metal migration · Lithium distribution

Introduction and motivation

Since their introduction in 1991 by Sony [1], lithium ion batteries (LIBs) became the preferential choice for electrochemical power sources for use in portable devices or as energy storage systems [2]. More recently, in order to replace conventional combustion engines, lithium ion batteries were successfully implemented in automotive applications, such as hybrid, plug-in, or electric vehicles [3, 4]. The success of LIBs can be attributed to their unique properties, such as high specific energy densities, stable cycling performance, high energy efficiency, and a low self-discharge rate [5]. The state-of-the-art lithium ion battery is consist of a positive (cathode) and a negative (anode) electrode and an electrolyte-soaked separator [6]. Intercalation electrodes, consisting of carbonaceous materials (e.g., graphite) combined with conductive agent and polymeric binder, are commercially used as anode materials. Carbonaceous-based electrodes offer the beneficial combination of desired properties such as low operating potential (0.025 V vs. Li/Li^+), a decent specific capacity (372 mAh/g), highly reversible lithium uptake/release, and high abundance. Apart from intercalation materials, different other candidates are under investigation, e.g., intermetallic compounds containing lithium (e.g., Si, Sn) and conversion materials (e.g., $ZnFe_20_4$, Mn_3O_4) [7, 8]. Furthermore, cathode materials are classified as insertion materials and can be divided into three groups, depending on their ability to conduct ions in one, two, or three spatial dimensions [9]. Olivine compounds $LiMPO_4$ (M = Fe, Mn, etc.) exhibit diffusion pathways in one dimension (1D), whereas layered transition metal oxides $LiMO_2$ (M = Co, Ni, Mn, etc.) and spinel compounds LiM_2O_4 (M = Mn, Ni, etc.) have the ability to conduct ions in two (2D) and three dimensions (3D), respectively [10]. As electrolyte, a non-aqueous mixture of cyclic and linear organic carbonates is used, in which a conducting salt (e.g., lithium hexafluorophosphate ($LiPF_6$)) is dissolved to ensure lithium ion conductivity [11, 12]. To achieve the desired properties, a wide variety of organic carbonates, such as ethylene carbonate (EC), propylene carbonate (PC), dimethyl carbonate (DMC), or diethyl carbonate (DEC), is used in

Published in the topical collection *Elemental and Molecular Imaging by LA-ICP-MS* with guest editor Beatriz Fernández García.

✉ Sascha Nowak
sascha.nowak@uni-muenster.de

[1] MEET Battery Research Center, Institute of Physical Chemistry, University of Münster, Corrensstraße 46, 48149 Münster, Germany

[2] Helmholtz-Institute Münster, IEK-12, Forschungszentrum Jülich GmbH, Corrensstrasse 46, 48149 Münster, Germany

different combinations [13, 14]. In detail, during the charging process, lithium ions migrate from the cathode to the anode and intercalate between the graphite layers, forming graphite intercalation compounds (GICs, $Li_{x-1}C_6$) and vice versa during discharge [15]. During the first cycle, the electrolyte is reduced at the anode surface, forming the solid electrolyte interphase (SEI) [16] and oxidized at the cathode forming the cathode electrolyte interphase (CEI) [16]. It consists of organic as well as inorganic decomposition products and consumes active lithium in the course of the formation [17]. However, the SEI forms a protective layer at every point of contact between graphite particles and the electrolyte, prohibiting further electrolyte reduction and thus capacity loss. Therefore, a uniform SEI is beneficial for a constant performance and long life span of lithium ion batteries [18].

One of the major issues of LIBs is a phenomenon called aging, invoked by degradation of different cell components. Consequently, aging leads to limited cycling performances resulting in a shortened LIB lifetime. While some aging processes, such as SEI formation, are essential, other degradation processes—e.g., electrolyte aging—are adverse for the performance and safety [19]. One part of aging is the so-called transition metal dissolution (TMD), migration and subsequent reductive deposition on the anode surface. The deposition of transition metals on the anode surface can lead to destruction of the SEI and therefore depletion of its protective properties [20, 21]. Possible origins of transition metal dissolution can be impurities in the cathode lattice, particle cracking induced by structural changes on atomic level, or structural changes due to phase transformation during the charge/discharge reaction. These causes were postulated for layered $Li_1[Ni_{1/3}Mn_{1/3}Co_{1/3}]$ (NMC111) cathodes [22]. TMD was also investigated for spinel-type materials for instance $LiNi_{0.5}Mn_{1,5}O_4$ (LNMO) and $LiMn_2O_4$ (LMO), however, exhibiting other degradation mechanism due to different chemical environment with respect to TM oxidation states [23, 24]. Due to these effects, induced by TMD, on the performance of numerous cell setups, suitable analytical techniques are necessary to investigate and understand this phenomenon. Recent reports showed the applicability of depth-resolved analysis techniques—in this case, LA-ICP-MS and glow discharge-mass spectrometry (GD-MS)—in the field of LIBs [25–27]. Lateral resolutions from the single- to the three-digit micrometer range can be achieved for LA-ICP-MS while depth resolutions below 1 μm are possible [28]. In comparison, common surface techniques in the field of LIBs are time of flight-secondary ion mass spectrometry (ToF-SIMS), X-ray photoelectron spectroscopy (XPS), or secondary electron microscopy with energy dispersive X-ray (SEM-EDX), which exhibit various drawbacks like small sample spots, lack in quantification, and prolonged measurement times [29–31]. Compared with these surface-sensitive techniques, LA-ICP-MS offers the ability to scan samples with a size of several square centimeters in a short period of time. Another significant advantage is the minimal effort in terms of sample preparation since no ultra-high vacuum is necessary. Despite these major advantages, LA-ICP-MS is so far not a well-established technique for the analysis of battery materials. This is mainly due to the complex and rough constitution of the samples itself. However, laser ablation was already implemented extensively in other fields of research, such surface analysis of biological samples, medical research, and geology [32–34].

This work reports on the ongoing development of a method to visualize transition metal dissolution (TMD) and lithium loss by means of laser ablation-inductively coupled plasma-mass spectrometry (LA-ICP-MS). Spatially resolved deposition patterns (Li, Mn, and Ni) can help to understand the mechanisms regarding TMD and lithium loss. For this, it is crucial that the obtained images have a good resolution. However, this often comes along with the cost of long measurement periods and high demand of resources, such as the carrier gas. Therefore, a substantial reduction of time and resource consumption is preferred, while preserving an adequate resolution. Resolution for LA bases imaging depends on numerous factors. Parameters, such as ablation spot size, lateral scanning speed of the LA, integration, and settling time of the utilized mass spectrometer, washout times, and many others influence the authenticity of the image. Extensive studies evaluating this problem have been published [33, 35]. Furthermore, graphite exhibits numerous properties that make for a very complex matrix for LA-ICP-MS measurements. Its rough surface in particular makes it difficult to archive optimal ablation conditions. Subsequently, this work deals with an empiric approach to evaluate influences on lateral resolution.

Experimental

Cell design and cyclic aging parameters

The cyclic aging experiments were carried out using a coin cell setup (2032, Hohsen Corporation, Japan) consisting of the casing (20 × 3.2 mm), a seal ring, a spacer, a spring, the two electrodes, and a separator. As cathode material, the spinel-type LNMO was used. The anode of choice was a hard carbon (HC)/mesocarbon microbeads (MCMB) composite electrode. One hundred microliters of a 1-M solution of LiPF6 in a mixture of ethylene and ethyl methyl carbonate (EC/EMC, 1:1 wt%, LP50, Selectilyte®, BASF, Germany) was used as electrolyte. Two different types of separators were used, both based on a non-woven fiber (Freudenberg FS2190) and thin polypropylene film (Celgard 2500), either with one or two layers of the thin film separator.

In order to induce uneven pressure conditions within the cell, resulting in inhomogeneous TMD pattern, the spacer that is responsible for an even pressure transmission from the spring to the electrode stack, was replaced by a metal washer of the same size.

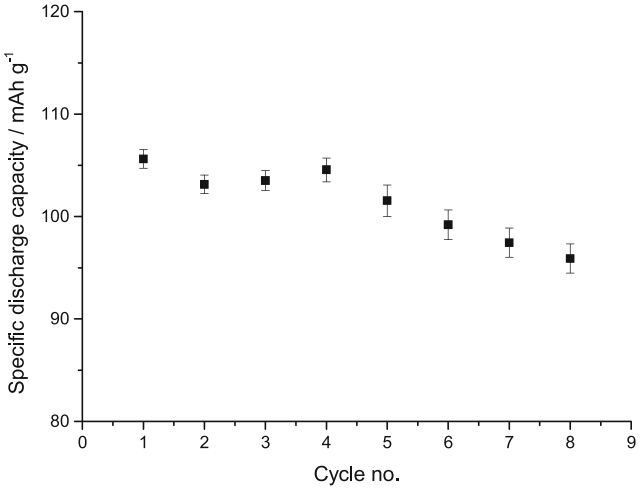

Fig. 1 Electrochemical cycling performance of a LNMO/(MCMB/HC) full cell: cycles 1–3: c-rate, 0.2; charge cut-off, 5.0 V; discharge cut-off, 3.0 V; cycles 4–8: c-rate, 0.5; charge cut-off, 5.1 V; cv-step, 2 h at 5.1 V; discharge cut-off, 3.0 V; electrolyte, 1 M $LiPF_6$ in EC/EMC (1:1 by weight); $n = 3$

To generate TMD, the cells were electrochemically cycled at a temperature of 20 °C using a Maccor series 4000 battery test system (Maccor, Inc., Tulsa, USA). A 2-h rest step prior to the electrochemical aging ensured an even electrolyte distribution within the electrodes. The charge/discharge aging was performed in a voltage window from 3.0 to 5.0 V exhibiting three formation cycles at 0.2 C with subsequent charge/discharge aging at elevated charge cut-off voltages of 5.1 V with an additional constant voltage step of 2 h over a period of 4 cycles.

After charge/discharge cyclic aging (Fig. 1), the cells were disassembled and the electrode of interest rinsed, using 500 μL of diethyl carbonate to remove residues of the conducting salt.

Mapping experiments

The mapping experiments were performed using a 193-nm ArF Excimer Laser (Analyte Excite Excimer LA-System, Teledyne Cetac, USA) coupled to an ICP-MS System (7700 Series, Agilent Technologies, USA). A moveable ablation cell, as well as camera and laser-focusing equipment provided motion in three dimensions.

Table 1 Evaluated combinations for elemental mapping via LA-ICP-MS

Combination	Lateral speed (μm/s)	Frequency (Hz)
A	110	10
B	220	20
C	330	30
D	440	40

Table 2 Laser settings for LA-ICP-MS mapping experiments

Parameter	(1) Optimisation	(2) Application
Laser setpoint (J)	1	7
Fluence (J cm^{-2})	0.17	2

The elements that were investigated are ^{7}Li, ^{55}Mn, and ^{60}Ni. The scans were performed using a circular ablation spot (110 μm in diameter). Different lateral scanning speeds were evaluated, ranging from 110 to 440 μm/s. The laser frequencies were adjusted with increasing scanning speeds, ranging from 10 to 40 Hz. The exact combinations are shown in Table 1.

Furthermore, different laser energy setting was used, depending on the performed measurement, as shown in Table 2.

Helium (99.9999%, Westfalen AG, Germany) was used as the laser-ablation carrier gas with a total gas flow of 900 mL/min (cell, 500 mL/min; cup, 400 mL/min).

Table 3 displays the utilized ICP-MS parameters.

Results and discussion

Transition metal dissolution

First, a reference measurement using a common spacer in the coin cell setup was performed in order to evaluate whether the applied aging parameters can induce TMD. This mapping served as a blank measurement to evaluate the influence of locally varying pressure conditions at a later stage.

The deposition patterns of ^{7}Li (Fig. 2a), ^{55}Mn (Fig. 2b), and ^{60}Ni (Fig. 2c) on the carbonaceous anode were visualized and evaluated with regard to the induced TMD. While Mn and Ni dissolution and subsequent deposition seemed to result in more inhomogeneous patterns, the distribution of ^{7}Li is more even. This observation verified that TMD occurs when using the applied cyclic aging parameters.

Transition metal dissolution inhomogeneity induced by pressure

By using a washer instead of a spacer, inhomogeneous TMD could be induced in shape of a circle (Fig. 3). Areas with less pressure, due to the hole in the middle

Table 3 ICP-MS parameters used for laser ablation investigation

Parameter	Value
RF power (W)	1550
RF matching (V)	1.30
Ar carrier gas flow (mL/min)	950
Integration time per mass (s)	0.03

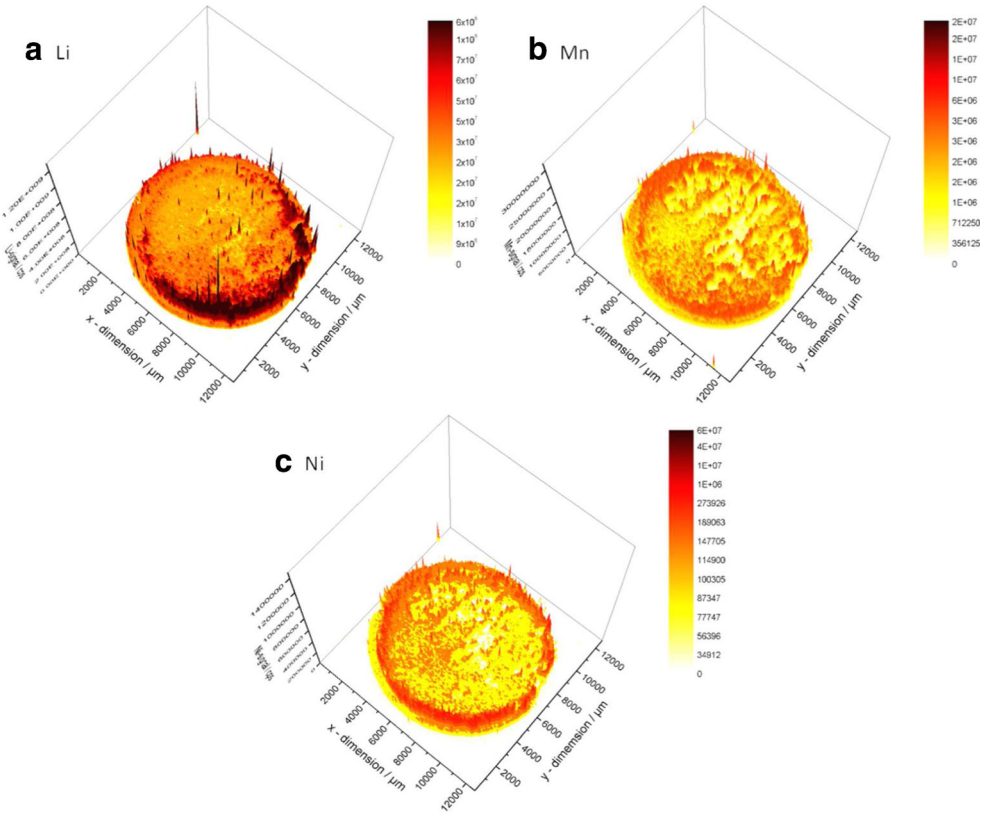

Fig. 2 The results of LA-ICP-MS mapping experiment visualizing **a** ^{7}Li-signal, **b** ^{55}Mn-signal, and **c** ^{60}Ni signal. Spot size, 110 µm (circular); scan speed, 110 µm/s; frequency, 10 Hz; laser energy, 2 J/cm^{2}; He gas flow, 900 mL/min. Ablated material: carbonaceous anode. Intensity units are given in counts per second (cps)

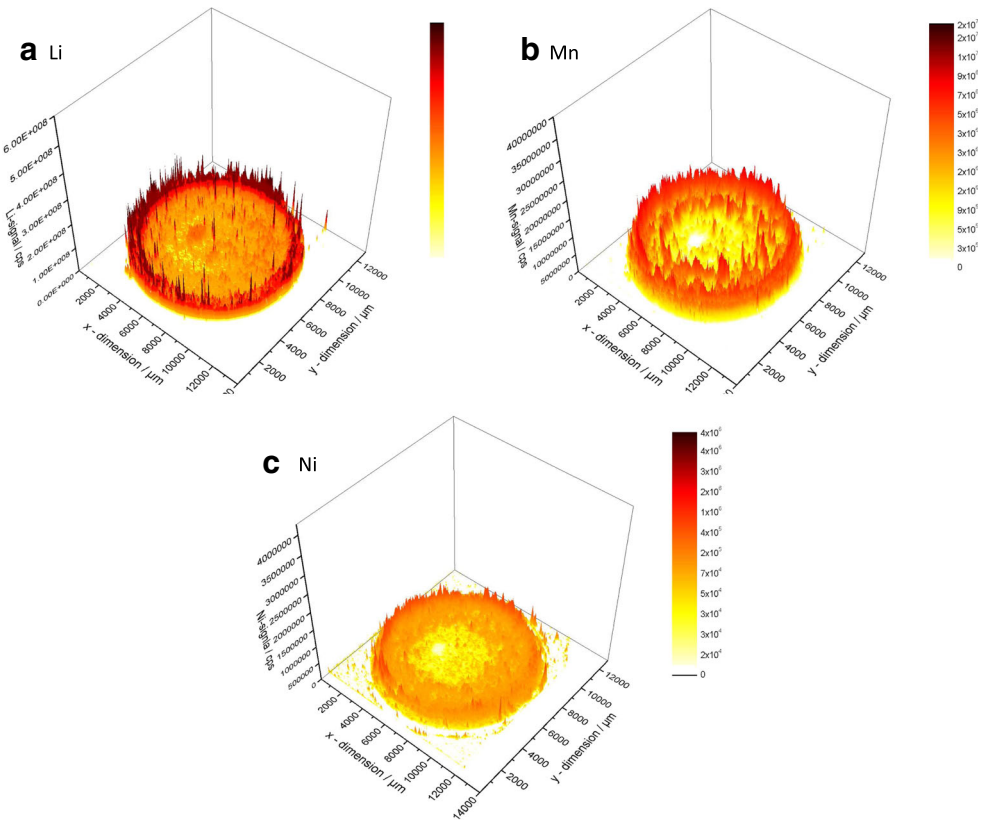

Fig. 3 The results of LA-ICP-MS mapping experiment visualizing **a** ^{7}Li-signal, **b** ^{55}Mn-signal, and **c** ^{60}Ni-signal. Spot size, 110 µm (circular); scan speed, 110 µm/s; frequency, 10 Hz; laser energy, 2 J/cm^{2}; He gas flow, 900 mL/min. Instead of a spacer, a washer was used. Ablated material: carbonaceous anode. Intensity units are given in counts per second (cps)

of the washer, experience less TMD and deposition on the anode. This effect might occur due to different diffusion pathways. In areas with higher pressure, anode and cathode have less distance to each other, resulting in shorter diffusion pathways for the measured elements. A second reason for the inhomogeneous deposition could be locally induced overcharges [26, 29]. Overall, this effect seemed to be more distinct for the transition metals ^{55}Mn and ^{60}Ni compared with the ^{7}Li signal.

Since it was a goal of this work to improve the measurement time without lacking in resolution, the "donut-shaped" deposition patterns were utilized to evaluate the improvement of the ablation parameters.

Evaluation of different scanning settings

The evaluation was carried out with very low laser energy settings (Table 2) to allow for multiple ablations on the same electrode and thus comparison of the images with different scanning speeds. Since all obtained signals were well above the LOD for the specific elements, qualitative results were achieved for all experiments.

Double ablation of cycled graphite anodes

To observe the influence of different scanning speeds, two ablations of the same electrode were carried out. Low energy

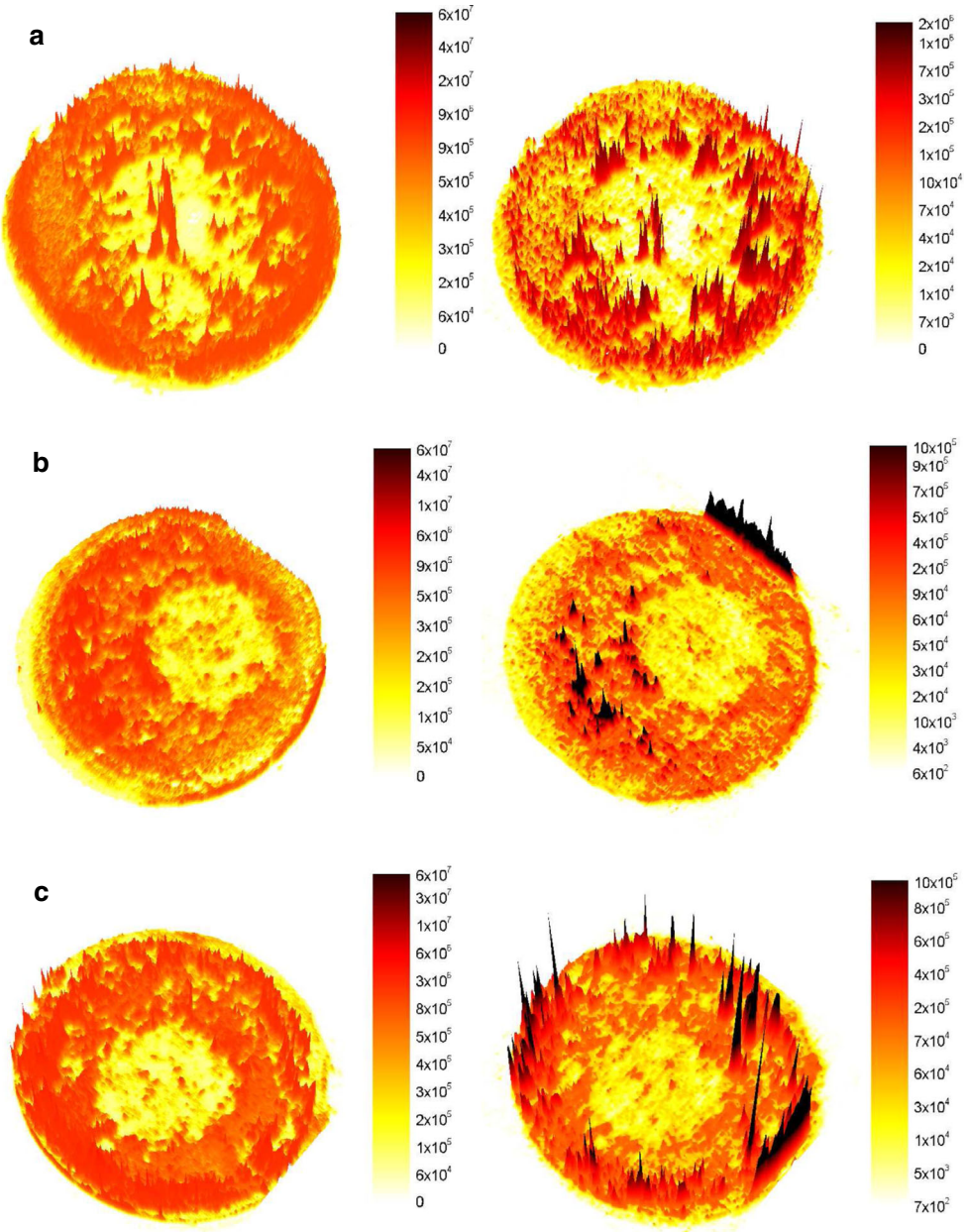

Fig. 4 The results of LA-ICP-MS mapping experiment visualizing the ^{55}Mn-signal with different lateral speeds and frequencies: **a** 110 μm/s, 10 Hz (left) and 220 μm/s, 20 Hz (right); **b** 110 μm/s, 10 Hz (left) and 330 μm/s, 30 Hz (right); **c** 110 μm/s, 10 Hz (left) and 440 μm/s, 40 Hz (right). All measurements were carried out using the following: laser energy, 2 J/cm^2; helium gas flow, 900 mL/min, 110 μm spot size (circular). Ablated material: carbonaceous anode. Intensity units are given in counts per second (cps)

Table 4 Measuring times for mapping of one electrode (12 mm in diameter) for the evaluated combinations A–D

Combination	Time per measured electrode (min)
A	260
B	156
C	121
D	103

settings were chosen to minimalize the diversion effects and the amount of ablated material, so that the same structures are still visible in the 2nd run. The first ablation of every electrode was done using a lateral speed of 110 µm/s and a frequency of 10 Hz. For the second ablation, combinations B to D (Table 1) were applied, respectively. In the following discussion, only Mn mappings are shown; however, the statements are valid for ^{60}Ni as well.

The obtained images for different scanning settings (Fig. 4) are compared regarding the influence on lateral resolution. The left image of every row shows the 1st ablation with a lateral speed of 110 µm/s and a frequency of 10 Hz, whereas the right image depicted the 2nd ablation using 220 µm/s and 20 Hz (Fig. 4a), 330 µm/s and 30 Hz (Fig. 4b), 440 µm/s, and 40 Hz (Fig. 4c), respectively.

Due to constant dwell times (Table 3) for all measurements, the generated pixels should theoretically increase in width for higher lateral speeds of the LA, whereas the resolution in y-direction stays the same for all measurements.

For all combinations, the patterns obtained for the 1st and 2nd ablations are very similar. To evaluate possible deviation between the washer hole and the displayed circular deposition, the widths are compared. Using the respective areas would be preferable; however, it is difficult to calculate these, due to the non-perfect circular shape of the deposition. For all images, a width between 5.0 mm (Fig. 4a, c) and 4.9 mm (Fig. 4b) can be observed, deviating from the hole widths in the washer (5.6 mm). Although the width changes among different electrodes, the discrepancies are within the margin of error. Furthermore, the diameter stays the same for the different scanning settings of the same electrode, thus not correlating with increasing scanning speeds. This suggests a phenomenon effecting the deposition to be responsible for differences between the widths, rather than deviation of the image due to measurement parameters. However, there are small differences between the applied combinations. With rising lateral speed and frequency, the visualization suffers in terms of resolution. In Fig. 4a, the observed hotspots (signals of high intensity) match well for both ablation runs. In Fig. 4b, c, these

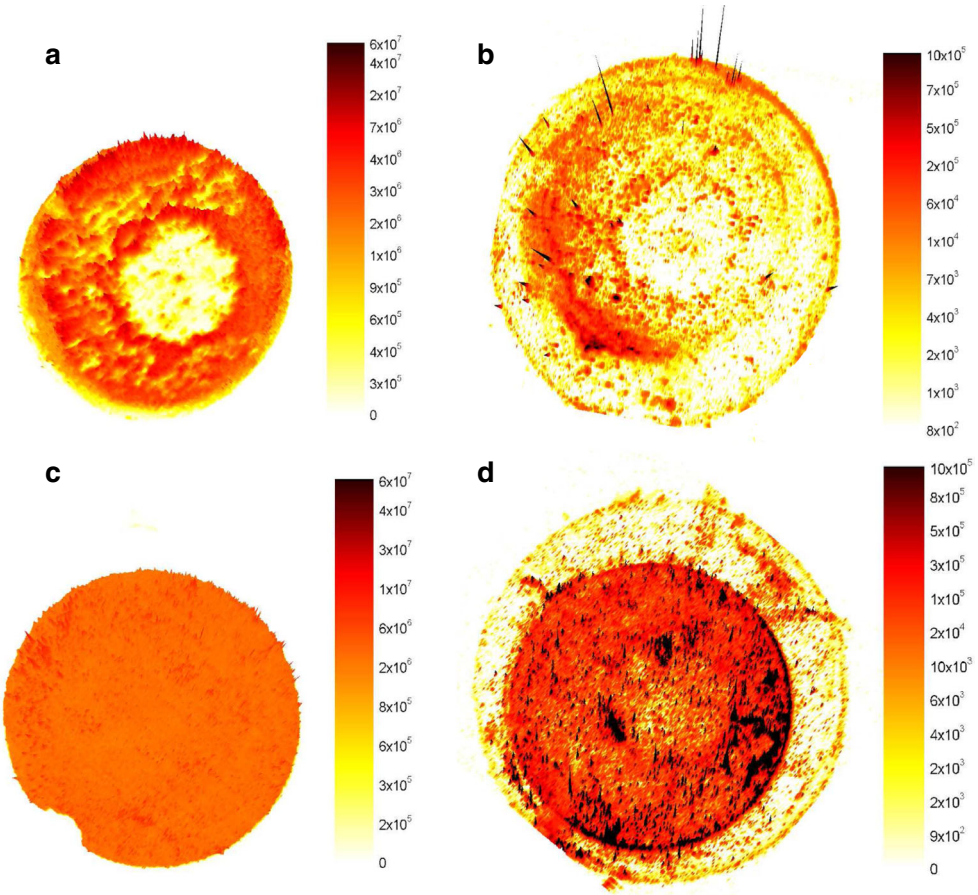

Fig. 5 The results of LA-ICP-MS mapping experiment visualizing the ^{55}Mn-signal: spot size, 110 µm (circular); scan speed, 440 µm/s; frequency, 40 Hz; laser energy, 2 J/cm^2; He gas flow, 900 mL/min. **a** Carbonaceous anode, **b** Celgard separator (anode side), **c** LNMO cathode, **d** Celgard separator (cathode side). Intensity units are given in counts per second (cps)

hotspots seem to be distorted and less distinct. However, the inhomogeneities induces by the washer are apparent for all three combinations.

Diversions between 1st and 2nd ablations can also be due to displacement or re-deposition of ablated matter induced by the laser sputtering process. Furthermore, transition metal deposition will only occur on the surface of the anode, resulting in possible absence of transition metals in ablation depth of the 2nd run. In addition, the rough surface of carbonaceous-based anodes impeded a completely smooth ablation via sputtering. However, there are no grave differences for any of the evaluated scanning speeds. Consequently, all evaluated settings are viable for mapping of carbonaceous anodes. This corresponds to savings of 61% in time and He consumption, when comparing combinations A and D (Table 4). Due to the significant savings of resources, future measurements will be carried out using the optimized method combination D (Table 1).

Comparison of cathode and separator TM deposition and distribution patterns

In addition, the applicability of the presented method was investigated for separators and the cathode. During cycling, a triple-layered separator was used to obtain samples for post-mortem analysis of the cathode and anode, respectively. Additionally, a separate analysis of the separators facing the anode or cathode was performed. In order to recognize the positions of the electrodes and separators during cyclic aging, they were marked after disassembly of the cell. All separator investigations were conducted using the thin polypropylene foil part.

Evaluation of the resulting images (Fig. 5) shows the expected TM deposition pattern on the anode (Fig. 5a), with less Mn in the lower pressure areas. Compared with the separator, that was facing the anode side (Fig. 5b), a matching imprint of the deposition pattern can be seen. However, for the cathode (Fig. 5c), no inhomogeneities are visible. The Mn distribution is smooth and homogeneous across the whole electrode. The separator facing the cathode (Fig. 5d) shows an imprint of the cathode as well. A circular area with slightly less transition metal, matching that of the anode, is observable. Nonetheless, this seems far less distinct than for the anode facing side. Overall, Fig. 5d shows significant more transition metal deposition. There are possible two reasons to explain this phenomenon: first, the transition metal ions initially passing through the cathode-facing separator, thus increasing the possibility for deposition; second, the high amount of transition metals could be due to physical attrition of cathode material onto the separator.

In general, this method could be successfully applied to separator analysis. However, due to low signal intensities, a higher laser energy might be required with the drawback of increasing the risk of melting the separators due to increased heat development during analysis.

Conclusion

In this study, LA-ICP-MS could be utilized to demonstrate the influence of different pressure conditions on TMD, by visualizing the TM deposition on carbonaceous anodes. Therefore, the standard spacer in a coin cell setup was replaced by a washer. The performed imaging measurements revealed an inhomogeneous deposition pattern that matched the dimension of the washer, depicted by the hole in the center. High-pressure areas suffer higher amounts of TMD, whereas for low pressure areas, less-intense signals could be observed. This effect could be explained by shorter diffusion pathways between anode and cathode. Furthermore, the increased pressure could result in locally higher overcharge potentials, thus inducing more TMD in the respective areas.

The displayed TMD patterns were used to estimate the influence of increased lateral scanning speeds and laser pulls frequencies on the spatial resolution of mapping experiments using LA-ICP-MS. All tested settings resulted in adequate images for the evaluation of TMD. However, with increasing scanning speeds, the resolution seems to decrease. Nonetheless, it is hard to determine whether these expected observations are solely due to the decreased amount of data points per line. Other effects, such as re-deposition of ablated material, element diversion, or differences in terms of surface conditions after one ablation run, may have different influences for varying ablation settings. Furthermore, a different ablation behavior of the complex and rough graphite matrix is possible.

In a proven principle study, the developed LA-ICP-MS method was applied to other parts of the battery system, namely the cathode and separator. Both were investigated concerning the TM pattern and their similarity to the deposition of the anode. To distinguish between anode and cathode TM patterns, separator parts facing the anode and cathode were investigated, respectively. The deposition pattern found on the anode surface could be matched to that of the separator facing its direction. On the cathodes, no distinguished pattern is observable; whereas, a slight inconsistency with circular shape can be seen on the respective separator surface. Overall, a high amount of transition metals is found on the cathode separator due to physical friction between cathode and separator.

To conclude, it can be stated that the developed method has been proven to be effective and significantly faster for mapping of anodes than with previously used settings. The obtained good resolution allowed the investigation of deposition patterns between electrodes and separator. However, different scan speeds, ablation spot sizes, and shapes should be evaluated in more detail.

Funding information The authors wish to thank the German Federal Ministry of Education and Research (BMBF) for funding this work in the project “Elektrolytlabor-4E” (03X4632) and the Ministry of Economic Affairs in North Rhine-Westphalia for funding the project “GrEEn” (W044A).

Compliance with ethical standards

Conflict of interest The authors declare that they have no conflict of interest.

References

1. Nagaura T. Progress in batteries and solar cells, vol. 10. Brunswick, OH: JEC Press Inc; 1991.
2. Wagner R, Preschitschek N, Passerini S, Leker J, Winter M. Current research trends and prospects among the various materials and designs used in lithium-based batteries. J Appl Electrochem. 2013;43:481–96. https://doi.org/10.1007/s10800-013-0533-6.
3. Schmuch R, Wagner R, Hörpel G, Placke T, Winter M. Performance and cost of materials for lithium-based rechargeable automotive batteries. Nat Energy. 2018;3:267–78. https://doi.org/10.1038/s41560-018-0107-2.
4. Patry G, Romagny A, Martinet S, Froelich D. Cost modeling of lithium-ion battery cells for automotive applications. Energy Sci Eng. 2015;3:71–82. https://doi.org/10.1002/ese3.47.
5. Armand M, Tarascon JM. Building better batteries. Nature. 2008;451:652–7. https://doi.org/10.1038/451652a.
6. Winter M, Brodd RJ. What are batteries, fuel cells, and supercapacitors? Chem Rev. 2004;104:4245–69. https://doi.org/10.1021/cr020730k.
7. Placke T, Kloepsch R, Dühnen S, Winter M. Lithium ion, lithium metal, and alternative rechargeable battery technologies: the odyssey for high energy density. J Solid State Electrochem. 2017;21:1939–64. https://doi.org/10.1007/s10008-017-3610-7.
8. Fichtner M. Komplexhydride, Metallfluoride: Konversionsmaterialien für die Energiespeicherung. Chemie Unserer Zeit. 2013;47:230–8. https://doi.org/10.1002/ciuz.201300604.
9. He P, Yu H, Li D, Zhou H. Layered lithium transition metal oxide cathodes towards high energy lithium-ion batteries. J Mater Chem. 2012;22:3680. https://doi.org/10.1039/c2jm14305d.
10. Meister P, Jia H, Li J, Kloepsch R, Winter M, Placke T. Best practice: performance and cost evaluation of lithium ion battery active materials with special emphasis on energy efficiency. Chem Mater. 2016;28:7203–17. https://doi.org/10.1021/acs.chemmater.6b02895.
11. Zhang SS, Jow TR, Amine K, Henriksen GL. LiPF6–EC–EMC electrolyte for li-ion battery. J Power Sources. 2002;107:18–23. https://doi.org/10.1016/S0378-7753(01)00968-5.
12. Schmitz RW, Murmann P, Schmitz R, Müller R, Krämer L, Kasnatscheew J, et al. Investigations on novel electrolytes, solvents and SEI additives for use in lithium-ion batteries: systematic electrochemical characterization and detailed analysis by spectroscopic methods. Prog Solid State Chem. 2014;42:65–84. https://doi.org/10.1016/j.progsolidstchem.2014.04.003.
13. Xu K. Nonaqueous liquid electrolytes for lithium-based rechargeable batteries. Chem Rev. 2004;104:4303–417. https://doi.org/10.1021/cr030203g.
14. Amereller M, Schedlbauer T, Moosbauer D, Schreiner C, Stock C, Wudy F, et al. Electrolytes for lithium and lithium ion batteries: from synthesis of novel lithium borates and ionic liquids to development of novel measurement methods. Prog Solid State Chem. 2014;42:39–56. https://doi.org/10.1016/j.progsolidstchem.2014.04.001.
15. Nowak S, Winter M. Elemental analysis of lithium ion batteries. J Anal At Spectrom. 2017;32:1833–47. https://doi.org/10.1039/C7JA00073A.
16. Kohs W, Santner HJ, Hofer F, Schröttner H, Doninger J, Barsukov I, et al. A study on electrolyte interactions with graphite anodes exhibiting structures with various amounts of rhombohedral phase. J Power Sources. 2003;119–121:528–37. https://doi.org/10.1016/S0378-7753(03)00278-7.
17. Agubra V, Fergus J. Lithium ion battery anode aging mechanisms. Materials (Basel). 2013;6:1310–25. https://doi.org/10.3390/ma6041310.
18. Winter M. The solid electrolyte interphase—the most important and the least understood solid electrolyte in rechargeable li batteries. Z Phys Chem. 2009;223:1395–406. https://doi.org/10.1524/zpch.2009.6086.
19. Grützke M, Kraft V, Hoffmann B, Klamor S, Diekmann J, Kwade A, et al. Aging investigations of a lithium-ion battery electrolyte from a field-tested hybrid electric vehicle. J Power Sources. 2015;273:83–8. https://doi.org/10.1016/j.jpowsour.2014.09.064.
20. Shin H, Park J, Sastry AM, Lu W. Degradation of the solid electrolyte interphase induced by the deposition of manganese ions. J Power Sources. 2015;284:416–27. https://doi.org/10.1016/j.jpowsour.2015.03.039.
21. Vetter J, Novák P, Wagner MR, Veit C, Möller KC, Besenhard JO, et al. Ageing mechanisms in lithium-ion batteries. J Power Sources. 2005;147:269–81. https://doi.org/10.1016/j.jpowsour.2005.01.006.
22. Evertz M, Horsthemke F, Kasnatscheew J, Börner M, Winter M, Nowak S. Unraveling transition metal dissolution of Li1.04Ni1/3Co1/3Mn1/3O2 (NCM 111) in lithium ion full cells by using the total reflection X-ray fluorescence technique. J Power Sources. 2016;329:364–71. https://doi.org/10.1016/j.jpowsour.2016.08.099.
23. Pieczonka NPW, Liu Z, Lu P, Olson KL, Moote J, Powell BR, et al. Understanding transition-metal dissolution behavior in $LiNi_{0.5}Mn_{1.5}O_4$ high-voltage spinel for lithium ion batteries. J Phys Chem C. 2013;117:15947–57. https://doi.org/10.1021/jp405158m.
24. Dong HJ, Shin YJ, Oh SM. Dissolution of spinel oxides and capacity losses in 4 V. J Electrochem Soc. 1996;143:2204–11. https://doi.org/10.1149/1.1836981.
25. Schwieters T, Evertz M, Mense M, Winter M, Nowak S. Lithium loss in the solid electrolyte interphase: Lithium quantification of aged lithium ion battery graphite electrodes by means of laser ablation-inductively coupled plasma mass spectrometry and inductively coupled plasma optical emission spectroscopy. J Power Sources. 2017;356:47–55. https://doi.org/10.1016/j.jpowsour.2017.04.078.
26. Schwieters T, Evertz M, Fengler A, Börner M, Dagger T, Stenzel Y, et al. Visualizing elemental deposition patterns on carbonaceous anodes from lithium ion batteries: a laser ablation-inductively coupled plasma-mass spectrometry study on factors influencing the deposition of lithium, nickel, manganese and cobalt after dissolution. J Power Sources. 2018;380:194–201. https://doi.org/10.1016/j.jpowsour.2018.01.088.
27. Evertz M, Schwieters T, Börner M, Winter M, Nowak S. Matrix-matched standards for the quantification of elemental lithium ion battery degradation products deposited on carbonaceous negative electrodes using pulsed-glow discharge-sector field-mass spectrometry. J Anal At Spectrom. 2017;32:1862–7. https://doi.org/10.1039/c7ja00129k.
28. Russo RE, Mao X, Mao SS. Peer reviewed: the physics of laser ablation in microchemical analysis. Anal Chem. 2002;74:70A–7A. https://doi.org/10.1021/ac0219445.
29. Börner M, Horsthemke F, Kollmer F, Haseloff S, Friesen A, Niehoff P, et al. Degradation effects on the surface of commercial $LiNi_{0.5}Co_{0.2}Mn_{0.3}O_2$ electrodes. J Power Sources. 2016;335:45–55. https://doi.org/10.1016/j.jpowsour.2016.09.071.
30. Kominato A, Yasukawa E, Sato N, Ijuuin T, Asahina H, Mori S. Analysis of surface films on lithium in various organic electrolytes. J Power Sources. 1997;68:471–5. https://doi.org/10.1016/S0378-7753(97)02592-5.

31. Peled E, Bar Tow D, Merson A, Gladkich A, Burstein L, Golodnitsky D. Composition, depth profiles and lateral distribution of materials in the SEI built on HOPG-TOF SIMS and XPS studies. J Power Sources. 2001;97–98:52–7. https://doi.org/10.1016/S0378-7753(01)00505-5.
32. Pozebon D, Scheffler GL, Dressler VL, Nunes MAG. Review of the applications of laser ablation-inductively coupled plasma mass spectrometry (LA-ICP-MS) to the analysis of biological samples. J Anal At Spectrom. 2014;29:2204–28. https://doi.org/10.1039/C4JA00250D.
33. Koch J, Günther D. Review of the state-of-the-art of laser ablation-inductively coupled plasma mass spectrometry. Appl Spectrosc. 2011;65:155–62. https://doi.org/10.1366/11-06255.
34. Chen L, Liu Y, Hu Z, Gao S, Zong K, Chen H. Accurate determinations of fifty-four major and trace elements in carbonate by LA-ICP-MS using normalization strategy of bulk components as 100%. Chem Geol. 2011;284:283–95. https://doi.org/10.1016/j.chemgeo.2011.03.007.
35. Günther D, Hattendorf B. Solid sample analysis using laser ablation-inductively coupled plasma mass spectrometry. TrAC Trends Anal Chem. 2005;24:255–65. https://doi.org/10.1016/j.trac.2004.11.017.